



# Visible-light-induced photodegradation of gas phase acetonitrile using aerosol-made transition metal (V, Cr, Fe, Co, Mn, Mo, Ni, Cu, Y, Ce, and Zr) doped TiO<sub>2</sub>

Siva Nagi Reddy Inturi<sup>a</sup>, Thirupathi Boningari<sup>a</sup>, Makram Suidan<sup>b,\*</sup>, Panagiotis G. Smirniotis<sup>a,\*\*</sup>

<sup>a</sup> Chemical Engineering Program, School of Energy, Environmental, Biological and Medicinal Engineering, University of Cincinnati, Cincinnati, OH 45221-0012, USA

<sup>b</sup> Engineering College and Architecture, American University of Beirut, Beirut 1107-2020, Lebanon



## ARTICLE INFO

### Article history:

Received 7 April 2013

Received in revised form 20 June 2013

Accepted 12 July 2013

Available online 22 July 2013

### Keywords:

Flame spray pyrolysis (FSP)

Titania (TiO<sub>2</sub>)

Visible-light-induced

Gas phase

Photodegradation

## ABSTRACT

A series of semiconductor photocatalysts based on transition metals (M' = V, Cr, Fe, Co, Mn, Mo, Ni, Cu, Y, Ce, and Zr) incorporated TiO<sub>2</sub> (Ti/M' = 20 atomic ratio) materials have been synthesized by adopting a one-step liquid flame aerosol synthesis technique. The resulting materials were explored for the destruction of acetonitrile in gas phase under visible light irradiation at ambient conditions. Our H<sub>2</sub>-TPR studies revealed the formation of Me—O—Ti bonds, which suggest the strong interaction of dopant metal-TiO<sub>2</sub> in all the as-synthesized materials. The reduction peaks in Cr-doped TiO<sub>2</sub> shifted to much lower temperatures, due to the increase in the reduction potential of titania and chromium. The strong interaction (formation of Cr—O—Ti bonds) is the main reason that the Cr/TiO<sub>2</sub> is an active photocatalyst in visible light. Our XPS studies suggest that the relative atomic percentage value of Ti<sup>3+</sup>/Ti<sup>4+</sup> characterized by XPS was significantly high for our flame-made Cr/TiO<sub>2</sub> nanoparticles (Ti<sup>3+</sup>/Ti<sup>4+</sup> = 0.89, 32.9%), whereas, other samples demonstrated poor atomic percentage value of Ti<sup>3+</sup>/Ti<sup>4+</sup> (Ti<sup>3+</sup>/Ti<sup>4+</sup> = 0.08–0.32). The existence of Ti<sup>3+</sup> species with narrow band gap is highly beneficial for the promotion of visible light-induced photocatalytic activity. The position of the Cr 2p peaks shifted to lower binding energies in Cr-doped TiO<sub>2</sub> nanoparticles. The electrons migrate from the TiO<sub>2</sub> nanoparticles to chromium species, which reveals a strong interaction between Cr and TiO<sub>2</sub> nanostructure in the interface of flame-made nanoparticles. Conversely, Mn<sup>3+</sup> species combined with TiO<sub>2</sub> because its surface metal dispersion was kept high after TiO<sub>2</sub> loading. However, Mn<sup>3+</sup> incorporated catalyst was inactive because of the small energy driving force for electrons to detrap from Mn<sup>2+</sup>. The UV-vis spectroscopy results of M'-doped TiO<sub>2</sub> (M' = Fe, Cr, V, Co, Ce, and Ni) materials showed augmentation of light absorption in the visible range. The Cr, V and Fe (Ti:M' atomic ratio = 20:1) titania aerosol catalysts reduced the bandgap energy of TiO<sub>2</sub> to 2.9 eV under visible light irradiation. Among all of the catalysts we tested, the transition metals (M' = Cr, Fe, and V) incorporated materials have shown an impressive catalytic performance in visible light. Among all the catalyst tested, Cr-doped titania demonstrated a superior catalytic performance and the rate constant is about 8–19 times higher than the rest of the metal doped catalysts. Their catalytic performances are correlated with the UV-vis spectrum of each synthesized catalyst to reveal the specific role played by each metal ion.

Published by Elsevier B.V.

## 1. Introduction

Photocatalytic treatment of polluted waters and gaseous streams has received enormous attention during recent years,

because of the potential application in environmental treatment and the synthesis of fine chemicals. It involves the utilization of ultraviolet or solar light by a semiconductor photocatalyst for abatement conditions [1–4]. Among the available semiconductors, the vast majority of current studies employed TiO<sub>2</sub> as the photocatalyst due to its stability and relatively low price along with its unique properties, such as high refractive index, excellent optical transmittance in the visible and near-infrared regions, high photo-chemical and corrosive resistance, high dielectric constant and photocatalytic activity [4–6]. However, the problem of low

\* Corresponding author.

\*\* Corresponding author. Tel.: +1 513 556 14 74; fax: +1 513 556 34 73.

E-mail addresses: [makram.suidan@uc.edu](mailto:makram.suidan@uc.edu), [msuidan@aub.edu.lb](mailto:msuidan@aub.edu.lb) (M. Suidan), [panagiotis.smirniotis@uc.edu](mailto:panagiotis.smirniotis@uc.edu) (P.G. Smirniotis).

energy efficiency of the photocatalytic process in solar light is what has hindered its practical application. It has become indispensable to bring the photocatalytic activity of  $\text{TiO}_2$  into visible spectrum and control the particle size of titania nanoparticles. During solar-light-induced photodegradation, the radiation from sun has minimal conversion efficiency for excitation of valence bond electrons. If at all excitation occurs, there is high electron-hole recombination. In addition, these drastic disadvantages involved with the conventional  $\text{TiO}_2$  catalysts prevent these photo-catalytic processes from being commercially applied. Both these concerns could be addressed synthetically with appropriate design of an anchoring functionality that could covalently bind the  $\text{TiO}_2$  surfaces very efficiently [7–11]. The doping of metal/metal oxides has enabled the formation of hybrid O 2p conduction band with lower band gap energy, favoring absorption over the whole visible spectrum [12–16].

On the other hand, conventional synthesis procedures suffer from the low yield in addition to the long processing time, especially for very fine and pristine nanoparticles. All these, necessitate the needs for large tanks and high energy equipment which in turn limits its flexibility in direct scaling-up. Additionally, they also incur additional costs in terms of production time, high energy consumption, floor space and waste disposal, which are subsequently reflected in the price of the final products. An increasingly popular alternative process is to synthesize fine nanoparticles in a single-step and without further processing. Examples of such technique include the flame aerosols [17,18], spray pyrolysis [17,19], furnace and plasma processing [20], laser ablation [21] and chemical vapor deposition [22]. In particular, the flame aerosol technique (FSP) is an established and elegant synthesis technique capable of producing inexpensive nanoparticles at industrial scale. At present, large scale production of simple nanoparticles is routinely achieved in a single step technique using a compact flame reactor design for (in descending order of production mass) carbon blacks, pigmentary titania, zinc oxide, fumed silica and optical fibers with an estimated annual production in the order of million metric tons [23]. An added benefit of FSP technique is being able to utilize a broader spectrum of liquid precursors so that even noble metal deposited  $\text{TiO}_2$  can be made in one step [17].

Acetonitrile is an extremely stable, volatile and toxic molecule present in various civil and industrial wastewaters. Acetonitrile is also detected as an in-door air component emitted by commercial fibrous polymeric materials, resins and smoking tobacco [24]. Acetonitrile is an interesting model molecule for photo-oxidation studies because it possesses an alkyl and a cyanide group that may undergo different oxidation routes.

In the present work we report, the synthesis of different transition metal modified  $\text{TiO}_2$  photocatalysts for the visible light photodegradation of acetonitrile using a flame spray pyrolysis (FSP) technique. All of the materials were characterized by various physicochemical techniques. Photocatalytic activity of different M'/Ti aerosol nanoparticles is evaluated for the degradation of acetonitrile in visible light. The doping of  $\text{TiO}_2$  nanoparticles with Cr, Fe and V exhibited better conversions in the visible region whereas, the incorporation of the other transition metals (Mn, Mo, Ce, Co, Cu, Ni, Y and Zr) showed an inhibition effect on the photocatalytic activity. Among all the M'/ $\text{TiO}_2$ , Cr modified  $\text{TiO}_2$  demonstrated a superior photocatalytic activity and the rate constant is about 8–19 times higher than the rest of the metal doped catalysts. Our XPS results suggested that the doping of  $\text{TiO}_2$  with chromium cations using flame spray pyrolysis technique leads to the production of  $\text{Ti}^{3+}$  species. The energy level of  $\text{Ti}^{3+}$  lies between the valence band and the conduction band of  $\text{TiO}_2$ , which could effectively promote the electrons in the new valence band (VB) to be excited to the conduction band of  $\text{TiO}_2$ . Therefore, the existence of  $\text{Ti}^{3+}$  species on the surface that makes

$\text{TiO}_2$  excited under visible illumination. The chromium nanoparticles could serve as trapping centers for electrons photo-induced in the conduction band of  $\text{TiO}_2$ , meanwhile leaving the holes in the valence band of  $\text{TiO}_2$ . These results imply that the migration of charges is prompted on the interface of metal-doped  $\text{TiO}_2$  flame-made nanoparticles and the recombination of photo-induced  $e^-/h^+$  pairs is suppressed by the well-known Schottky barrier effect, which will contribute to the enhancement of photocatalytic activity in the visible region.

## 2. Experimental

### 2.1. Catalysts preparation

The synthesis procedure for the flame-made nanoparticles is explained in detail in our previous studies [25–29]. Briefly, a mixture of O-xylene (Sigma-Aldrich Reagent, 99%)/acetonitrile (Sigma-Aldrich Reagent) in the volume ratio of 3/1 is used as the solvent. For pure FSP made titanium-tetra-isopropoxide (TTIP, Sigma-Aldrich, purity N 97%) was used as precursor and diluted with the solvent to a 0.5 M solution metal oxide nanoparticles were synthesized by a one-step FSP synthesis technique. Precursor solutions resulting in powders of transition metal incorporated  $\text{TiO}_2$  were prepared by dissolving predetermined amounts of TTIP and metal precursor (chromium(III) 2-ethylhexanoate (Strem, 70% Cr in mineral spirits), vanadium(V) tri-*i*-propoxy oxide (Strem, ~98% V), iron(III) naphthenate (Strem, 80% Fe in mineral spirits), manganese(III) naphthenate (Strem, 56% Mn in mineral spirits), nickel(III) naphthenate (Strem, 60% Ni in toluene), copper(II) 2-ethylhexanoate (Strem, 16–19% Cu solvent free), cobalt 2-ethylhexanoate (Strem, 65% Co in mineral spirits), molybdenum 2-ethylhexanoate (Strem, 15% Mo), zirconyl 2-ethylhexanoate (Strem, 6% Zr in mineral spirit) and yttrium(III) naphthenate (Strem, 60% Y in toluene) such that the atomic ratios of Ti/M' is 20. The total molar concentration of Ti + M' (transition metal) in the liquid precursor was set at 0.5 M. During FSP, the liquid precursor was fed through a spray nozzle at a flow rate of 3 mL min<sup>-1</sup> using a syringe pump (Cole Parmer, 74900 series), where it was dispersed by a surrounding 5 L min<sup>-1</sup> flow of O<sub>2</sub> (1.5 bar, Wright Brothers, 99.98%). Combustion of the dispersed droplets was ignited by a surrounding supporting flame (premixed 1.0 L min<sup>-1</sup> O<sub>2</sub>/1.0 L min<sup>-1</sup> CH<sub>4</sub>). Additional 3 L min<sup>-1</sup> sheath O<sub>2</sub> (BOC Gases) was issued through the outer most sintered metal ring. Fine aerosol nanoparticles leaving the flame were collected on a flat glass fiber filter (Whatman GF/A, 150 mm in diameter) aided by a vacuum pump (Grainger Inc.). The aerosol nanoparticles were scraped from the filter for direct use as catalyst without any further treatment. The metal components of the catalysts are denoted Ti/M'.

### 2.2. BET surface area and pore volume measurements

The BET specific surface area of the as-prepared nanoparticles was determined from nitrogen adsorption equilibrium isotherms at liquid nitrogen temperature (77 K) using an automated gas sorption system (Micromeritics ASAP 2010) operating in continuous mode. Prior to the analysis, 0.050 ± 0.005 g of catalyst were evacuated under helium atmosphere for 3 h at 250 °C in the degassing port of the instrument. The adsorption isotherms of nitrogen were collected at 77 K using approximately six values or relative pressure ranging from 0.05 to 0.99 and by taking 0.162 nm<sup>2</sup> as the molecular area of the nitrogen molecule. The BET-equivalent diameter was calculated as  $d_{\text{BET}} = 6/(\rho \times \text{SSA})$  where  $\rho$  is the mass-weighted density of the powder ( $\rho_{\text{anatase}} = 3.84 \text{ g/cm}^3$  and  $\rho_{\text{rutile}} = 4.26 \text{ g/cm}^3$ ).

### 2.3. X-ray diffraction

The powder X-ray diffraction (XRD) patterns were employed for the identification of phases of the synthesized metal oxide nanoparticles. The XRD patterns were recorded on a Phillips Xpert diffractometer using nickel-filtered Cu K $\alpha$  (wavelength 0.154056 nm) radiation source and a scintillation counter detector. An aluminum holder was used to support the catalyst samples. The intensity data were collected over a 2 $\theta$  range of 10–80° with a step size of 0.025° and a step time of 0.50 s. Crystalline phases were identified by comparison with the reference data from International Center for Diffraction Data (ICDD) files.

### 2.4. UV-vis spectra

The catalyst powders were characterized with a UV-vis spectrophotometer (Shimadzu 2501PC) with an ISR1200 integrating sphere attachment for their diffuse reflectance with the wavelength ranging from 200 to 900 nm. BaSO<sub>4</sub> was used as the standard for these measurements.

### 2.5. Temperature programmed reduction ( $H_2$ -TPR)

$H_2$ -TPR of as-prepared aerosol nanoparticles was performed using an automated catalyst characterization system (Micromeritics model AutoChem 2910). Prior to the analysis approximately 0.050 g of the catalysts were pre-treated at 200 °C for 2 h in ultra high pure helium (30 mL min<sup>-1</sup>) stream. A mixture of isopropanol and liquid nitrogen was used in the trapper to collect the formed water during the TPR experiment. After preheating, samples were tested by increasing the temperature from 50 to 700 °C. The temperature was then kept constant at 700 °C until the signal of hydrogen consumption returned to the initial values. The temperature programmed reduction runs were carried out with a linear heating rate (10 °C/min) in a flow of 10%  $H_2$  in argon with a flow rate of 20 mL min<sup>-1</sup>. The hydrogen consumption was measured quantitatively by a thermal conductivity detector.

### 2.6. X-ray photoelectron spectroscopy (XPS)

The X-ray photoelectron spectroscopy (XPS) experiments were carried out on a Pyris-VG thermo scientific X-ray photoelectron spectrometer system equipped with a monochromatic AlK $\alpha$  (1486.7 eV) as a radiation source at 300 W under UHV ( $6.7 \times 10^{-8}$  Pa). Sample charging during the measurement was compensated by an electron flood gun. The electron takeoff angle was 45° with respect to the sample surface. The spectra were recorded in the fixed analyzer transmission mode with pass energies of 89.45 and 35.75 eV for recording survey and high resolution spectra, respectively. The powdered catalysts were mounted onto the sample holder and evacuated overnight at room temperature at a pressure on the order of 10<sup>-7</sup> Torr.

### 2.7. Photocatalysis

The photocatalytic reactor (Fig. 1) is made of quartz tube with inner diameter of 6 mm and length of 1 ft. The cooling jacket around the reactor effectively precluded IR part of the spectra from penetrating into the reactor and helps in cooling the lamps along with maintaining constant reactor temperature. Six 8 W fluorescent white light lamps (Wiko F8T5 W) were used as visible light source. Along with wooden housing coated with aluminum foil for better utilization of light due to reflection. Acrylic OP2 sheets were used to filter UV light. The catalyst was deposited onto the internal surface of the reactor by using 5 wt% of catalyst slurry. This slurry was made with distilled water after it was mechanically stirred

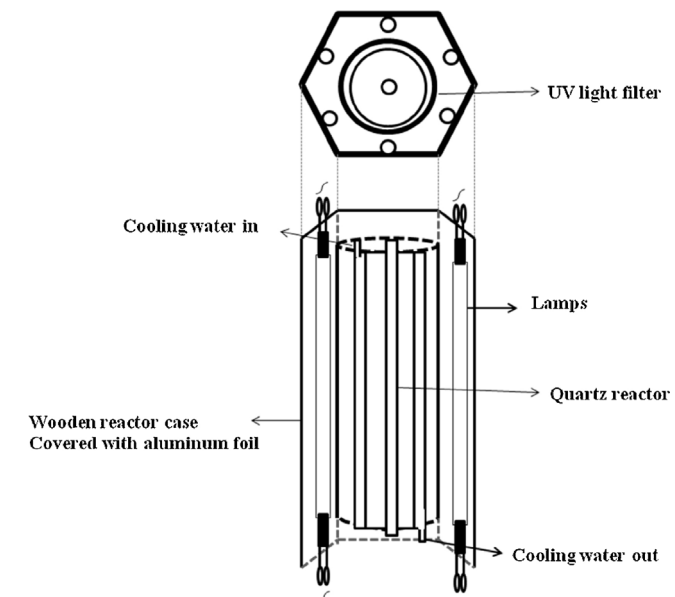


Fig. 1. Schematic representation of the reactor set-up.

overnight followed by ultrasonication for 60 min for elimination of any agglomerates present in the slurry. The reactor vessel was repeatedly rinsed with the catalyst slurry with each rinse followed by drying at 120 °C for 2 h. The weighted catalyst was 0.06 g corresponded to the catalyst loading of 5.8 mg TiO<sub>2</sub> per cm<sup>2</sup> of irradiated reactor surface.

The probe chemical (acetonitrile) was mixed with water in 1:3 volume ratios. Appropriate flow of air was maintained through the inlet of the reactor. The liquid reactant was fed through a spray nozzle at a flow rate to maintain the concentration of the inlet to the reactor as 500 ppm using a syringe pump (Cole Parmer, 74900 series). Small portion of the mixing section before inlet of the reactor was kept at 150 °C to vaporize the liquid reactant. The temperature in the reactor was determined by heat release of the lamps and varied from 30 °C at the reactor bottom to 33 °C at the reactor top. The reactor effluent is directed into a gas-sampling valve of a QP5050A GC-MS (Shimadzu) to analyze the products.

## 3. Results and discussion

### 3.1. X-ray diffraction

The powder X-ray diffraction patterns of various transition metals modified titania are shown in Figs. 2 and 3. The diffractogram patterns of pure TiO<sub>2</sub> (Degussa P25) are also presented for comparison purpose. For FSP TiO<sub>2</sub> and P25 sample, the strong characteristic peaks of titania (typically at  $d = 3.54$ , 1.90, and 2.40 Å, which correspond to anatase phase (JCPDS #71-1169) can be observed. In order to compare the effects of metal-ion doping on the anatase–rutile phase transformation, the fraction of rutile,  $X_R$  was calculated from the respective peak intensities using the following equation:

$$X_R(\%) = \left( 1 - \frac{1}{1 + (1.26 \times I_R/I_A)} \right) \times 100 \quad (1)$$

where  $I_R$  and  $I_A$  are the X-ray intensities of the rutile (1 0 1) and anatase (1 1 0) peaks, respectively. These relative rutile and anatase fractions are listed in Table 2, the ionic radii of the dopants also exhibited evidence of a rutile phase. The rutile fractions of P25 and FSP TiO<sub>2</sub> were estimated from Eq. (1) to be 19% of the FSP TiO<sub>2</sub> and transition metal-incorporated TiO<sub>2</sub> samples exhibited higher rutile

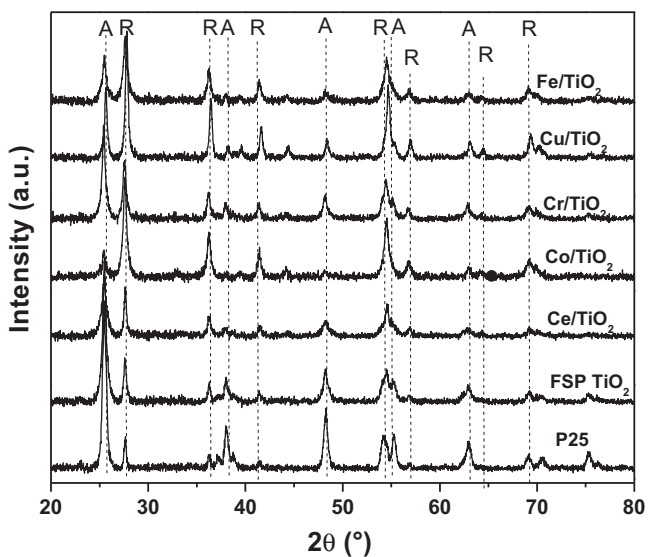


**Fig. 2.** Powder X-ray diffraction patterns of P25, FSP TiO<sub>2</sub> and M'/TiO<sub>2</sub> (M' = Ce, Co, Cr, Cu and Fe) catalysts made by FSP; (A → anatase and R → rutile TiO<sub>2</sub>).

fractions when compared to the flame-made TiO<sub>2</sub> nanoparticles. Interestingly, our XRD studies of M/TiO<sub>2</sub> (M = Cr, Fe, Co, Mn, Mo, Ni, Cu, Y, Ce, and Zr) samples revealed that the promoter oxides do play an important role in titania phase transformation. Only V/TiO<sub>2</sub> does not undergo any phase transformation. However, the intensities of the peaks of the M/TiO<sub>2</sub> were lower than those found for FSP TiO<sub>2</sub> or P25. This can be attributed to the presence of foreign ions in the catalyst [31]. No characteristic peak attributed to transition metal oxides was found in the XRD patterns. These results suggest that the doping levels we employed did not induce the formation of discrete impurity phases and that the metal ion appears to have been integrated into the basic structure of TiO<sub>2</sub>. However, it is conceivable that metal impurities, which were formed during synthesis, were nanoscopic or possibly dispersed on the surface. Thus, the crystal structure of TiO<sub>2</sub> indicates a mixture of anatase and rutile for all the as-synthesized metal-doped TiO<sub>2</sub> samples. Therefore, it is interesting to note that the transition metal dopants promoted the anatase to rutile phase transformation of TiO<sub>2</sub>. Some of the metal ion dopants such as V, Cr, Fe, Co, Mn and Ni ions are most likely

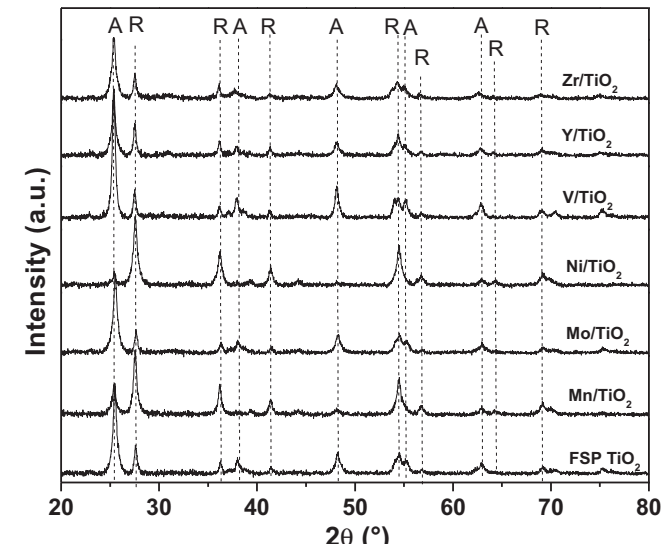


**Fig. 3.** Powder X-ray diffraction patterns of FSP TiO<sub>2</sub> and M'/TiO<sub>2</sub> (M' = Mn, Mo, Ni, V, Y and Zr) catalysts made by FSP; (A → anatase and R → rutile TiO<sub>2</sub>).

to be substituted at Ti<sup>4+</sup> sites within TiO<sub>2</sub> because ionic radii of dopants are similar to that of Ti<sup>4+</sup> (0.745 Å), whereas some other metal dopants such as Co, Cu, Mo, Y, Ce and Zr ions are possibly located in interstitial positions of the lattice rather than directly in Ti<sup>4+</sup> sites because of the relatively large size difference between dopants ions and Ti<sup>4+</sup>. However, Y, Ce and Zr ions seem to be larger than the pore diameter of the titania to be incorporated in TiO<sub>2</sub> lattice and thus, they are more likely to be found as dispersed metal oxides within the crystal matrix or they are dispersed on the surface of TiO<sub>2</sub>.

The X-ray powder diffraction patterns are also used to determine the crystallite size of all the prepared samples. The crystallite size  $\tau$  is determined from the broadening of the peaks by Scherrer's formula [30]:

$$\tau = \frac{K\lambda}{\beta_{\tau} \cos \theta} \quad (2)$$

where  $K$  is the shape factor = 0.9;  $\beta_{\tau}$  is the width of the peak at half the maximum intensity (FWHM) after subtraction of instrumental noise and  $2\theta$  is the diffraction angle. The estimation shows that the mean crystal size of the anatase TiO<sub>2</sub> individual particles calculated from Eq. (2) was 22–50 nm. Ce, Y, Zr and Mo have reduced the anatase crystal size from 28 nm where other metals have increased the crystal size up to 50 nm. On the other hand, in the case of rutile a significant increase in crystallite size was observed. The mass weighted average particle diameter has showed that the incorporation of other metal ions have increased the average particle size.

### 3.2. BET surface area and pore volume measurements

The major surface characterization results determined using nitrogen adsorption and desorption isotherms of the materials are summarized in Table 1. The BET surface area of the FSP synthesized TiO<sub>2</sub>, was determined to be 101 m<sup>2</sup>/g. In comparison, the surface area of the commercial product, Degussa P25 TiO<sub>2</sub>, is listed at 50 m<sup>2</sup>/g and confirmed by our measurements. One can observe that the presence of transition metal ions (such as Ce, Cr, Ni, Fe, Mn, Ni, and Y) have slightly lowers the surface area (SA) of the resulting catalyst (for example, SA: 101 m<sup>2</sup>/g for FSP TiO<sub>2</sub>, and SA: 98 m<sup>2</sup>/g for Cr/TiO<sub>2</sub>). The SA of Zr and Mo incorporated TiO<sub>2</sub> have showed slight improvement in their SA. The pore size also changes with the introduction of the transition metal. The vanadia forms a shell like structure onto a TiO<sub>2</sub> core rather than a solid solution of V atoms in the TiO<sub>2</sub> matrix in a flame, thereby increasing the VO<sub>x</sub> surface population density with decreasing SA [32]. The size of the metal ions for incorporation can also affect the pore formation during synthesis and, in turn, influence the pore quality. The pore volume of TiO<sub>2</sub> also decreases with the loading of transition metal as expected. This is a logical conclusion of the loss of surface area caused by partial blockage of the pores.

### 3.3. UV-vis spectra

To ascertain the capability of each particular transition metal modified titania to photodegrade organic chemicals in the visible range of spectrum, one needs to analyze the UV-vis diffuse reflectance spectra (Fig. 4). Degussa P25 TiO<sub>2</sub> is characterized by sharp absorption edges at about 400 nm ( $E_g \sim 3.11$  eV). However, the FSP TiO<sub>2</sub> has the absorption of about 403 nm ( $E_g \sim 3.08$  eV) this may be attributed to the reduction in the particle size. Most of the M-TiO<sub>2</sub> (M = V, Cr, Fe, Co, Mn, Ni and Cu) samples show extended absorption spectra into visible region in the range of 400–700 nm. Fig. 4 shows the TiO<sub>2</sub> samples doped with Zr, Mo, Y, and Ce ions exhibited relatively small absorption only between 400 and 500 nm, while the Co, Fe, Cu, Mn, V, Ni, or Cr-doped TiO<sub>2</sub>

**Table 1**Characterization results for transition metal incorporated  $\text{TiO}_2$  made by flame aerosol pyrolysis method.

Catalyst	Surface area analysis					X-ray diffraction analysis			
	Isotherm type <sup>a</sup>	SSA ( $\text{m}^2/\text{g}$ )	$d_{\text{BET}}^{\text{b}}$ (nm)	Pore volume ( $\text{cm}^3/\text{g}$ )	Pore diameter (nm)	$X_{\text{Anatase}}^{\text{c}}$ (%)	$d_A^{\text{d}}$ (nm)	$d_R^{\text{d}}$ (nm)	$d_{\text{xrd}}^{\text{e}}$ (nm)
P25	IV	51	30	0.18	30	80	30	158	56
FSP $\text{TiO}_2$	IV	101	15	0.29	15	81	28	125	47
Ce/ $\text{TiO}_2$	IV	98	15	0.30	15	48	22	138	82
Co/ $\text{TiO}_2$	IV	83	17	0.22	17	16	35	85	77
Cr/ $\text{TiO}_2$	IV	91	16	0.30	16	56	31	97	60
Cu/ $\text{TiO}_2$	IV	60	24	0.15	24	29	42	122	99
Fe/ $\text{TiO}_2$	IV	94	16	0.27	16	35	26	74	57
Mn/ $\text{TiO}_2$	IV	89	16	0.26	16	25	27	90	75
Mo/ $\text{TiO}_2$	IV	108	14	0.42	14	74	24	127	51
Ni/ $\text{TiO}_2$	IV	90	16	0.26	16	12	50	74	71
V/ $\text{TiO}_2$	IV	74	21	0.20	21	80	35	138	55
Y/ $\text{TiO}_2$	IV	91	16	0.24	16	64	26	130	63
Zr/ $\text{TiO}_2$	IV	100	15	0.29	15	71	24	118	55

<sup>a</sup> Isotherm type is based on IUPAC nomenclature.<sup>b</sup>  $d_{\text{BET}}$  is calculated based on mass weight average density of anatase and rutile phases determined by XRD.<sup>c</sup>  $X_{\text{Anatase}}(\%) = 100 - X_{\text{Rutile}}(\%)$ .<sup>d</sup>  $d_A$  and  $d_R$  are the crystallite sizes of anatase and rutile, respectively.<sup>e</sup>  $d_{\text{xrd}}$  is the mass weighted average particle diameter.

samples showed substantial and broader absorption shoulders up to 700 nm.

The enhanced absorption observed for the M- $\text{TiO}_2$  samples doped with Fe, Cr, V, Co, Ni, and Cu in visible region can be considered to involve the excitation of the 3d electrons of the dopant ion to  $\text{TiO}_2$  conduction band according to their respective energy levels [33–35]. The metal-ion dopants used in this study have different valence states than  $\text{Ti}^{4+}$  and, as a consequence, may induce the generation of oxygen vacancies during synthesis. The generation of new energy levels due to the injection of impurities within the bandgap coupled with the generation of oxygen vacancies by metal ion doping may contribute to the observed visible-light absorption of the M- $\text{TiO}_2$  samples.

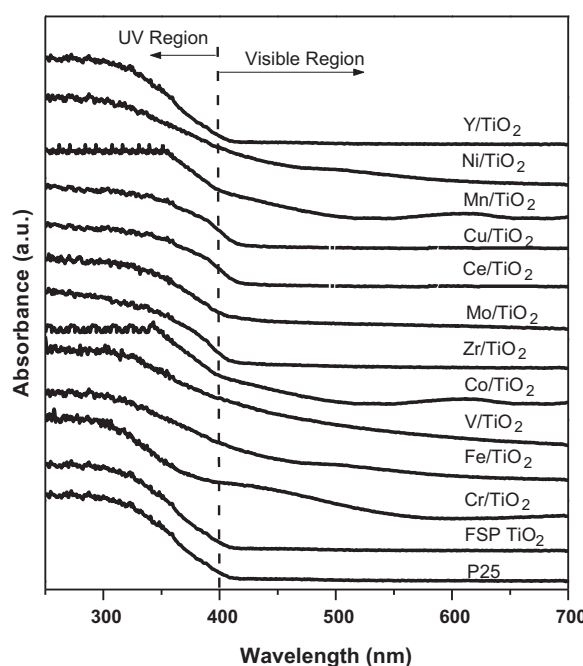
### 3.4. Temperature-programmed reduction ( $\text{H}_2$ -TPR)

In the present study, the reducibility of flame-made metal doped  $\text{TiO}_2$  samples was investigated by the quantitative  $\text{H}_2$ -TPR

(Fig. 5 and Table 2) to ensure the oxidation states of different metal incorporated  $\text{TiO}_2$  and relate these oxidation states with the photocatalytic activity studies of the catalysts. To maintain the crystal structure of the catalyst no TPR run was extended above 700 °C. The TPR profiles for all the transition metal incorporated  $\text{TiO}_2$  materials and their reduction profiles and total hydrogen consumption are given in Fig. 5 and Table 2, respectively. The total hydrogen consumption and reduction temperature for the catalyst are expressed in Table 2. One can observe that the reduction behavior of each transition metal incorporated  $\text{TiO}_2$  was quite different from the others. As shown in Fig. 5, the TPR profiles of most of the transition metal incorporated  $\text{TiO}_2$  materials showed more than one reduction transition peaks. These peaks are not clearly separated because of differences caused by metal dispersion, particle size, and the interaction between  $\text{TiO}_2$  and the metal oxide species.

From the TPR peaks we can observe a broad shoulder peak in the range 180–220 °C which corresponds to the dehydroxylation of the  $\text{TiO}_2$  surface and also the partial reduction of titania from  $\text{Ti}^{4+}$  to  $\text{Ti}^{3+}$  [36]. The single peak for the Ce/ $\text{TiO}_2$  is due to the oxygen removed in roughly to one-electron transfer per  $\text{CeO}_2$ . This indicates that the reduction of  $\text{Ce}^{4+}$  to  $\text{Ce}^{3+}$  occurs at 488 °C. For low amounts of Ce loading the secondary peak corresponding to high temperature is not observed [37]. For Co/ $\text{TiO}_2$  sample, the peak at 560 °C can be assigned to the overlap of two-step reduction of  $\text{Co}_3\text{O}_4$  to  $\text{CoO}$  and then to  $\text{Co}^0$  due to the reduction of metal oxides on the support [38]. Under TPR conditions, the two reduction peaks based on the two-step reduction may or may not be observed. The presence of only one reduction peak during TPR for the sample indicates that no residual cobalt remained on the samples under the temperature conditions used during the preparation of catalysts. Reduction of cobalt species ( $\text{Co}^{3+} \rightarrow \text{Co}^{2+}$ ) at temperatures higher than 500 °C indicates the strong interaction of cobalt with the surface. The strong interaction between Co metal and support depends on the size of cobalt oxide species.

The reduction temperatures of Cr/ $\text{TiO}_2$  are due to the strong interaction between Cr and  $\text{TiO}_2$  (Cr–O–Ti). The reduction profiles of bulk  $\text{CrO}_3$  comprise of the reduction peaks at 280, 462, and 585 °C. These peaks can be ascribed to the stepwise reduction of  $\text{Cr}^{6+} \rightarrow \text{Cr}^{5+}$ ,  $\text{Cr}^{5+} \rightarrow \text{Cr}^{3+}$  and  $\text{Cr}^{3+} \rightarrow$  either  $\text{Cr}^{2+}$  or  $\rightarrow$  the metallic state, respectively [39]. The reduction profile peaks of our Cr/ $\text{TiO}_2$  catalyst appeared at 265, 441, and 538 °C. The first peak at 265 °C is due to the partial hydroxylation and reduction of  $\text{TiO}_2$  along with the reduction of  $\text{Cr}^{6+}$  to  $\text{Cr}^{5+}$ , while the later are for the reduction of  $\text{Cr}^{5+} \rightarrow \text{Cr}^{3+}$  and  $\text{Cr}^{3+} \rightarrow$  either  $\text{Cr}^{2+}$  or  $\rightarrow \text{Cr}^0$ . The reduction

**Fig. 4.** UV-vis diffuse reflectance spectra of the transition metal modified  $\text{TiO}_2$ .

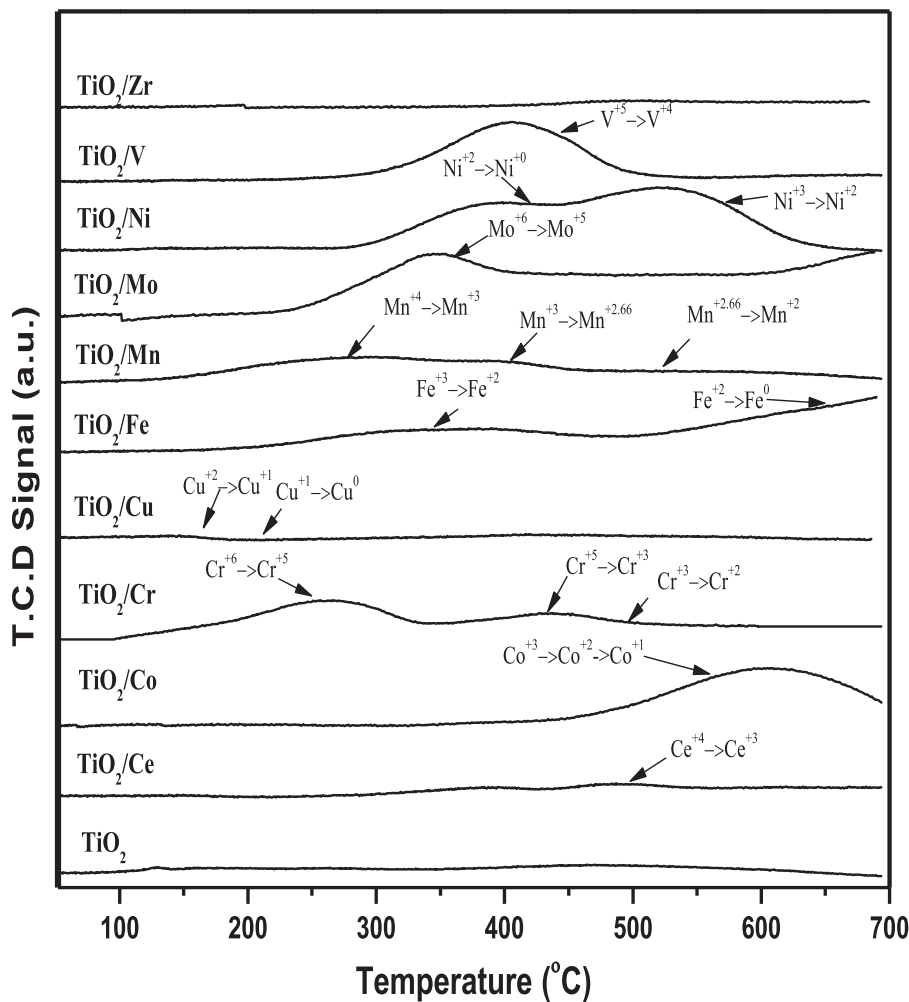


**Fig. 5.** H<sub>2</sub>-TPR patterns of M'/TiO<sub>2</sub> (M' = Ce, Co, Cr, Cu, Fe, Mn, Mo, Ni, V and Zr); 20 = Ti/M' atomic ratio (reduction temperature range 50–700 °C).

transition at 265 °C attributed to Cr<sup>6+</sup> → Cr<sup>5+</sup> which is made possible by the interaction between Cr and TiO<sub>2</sub>. The strong interaction (formation of (Cr—O—Ti) bonds) is the main reason that Cr/TiO<sub>2</sub> is an active photocatalyst in visible light [12].

The reduction profile of Cu/TiO<sub>2</sub> is characterized by two reduction peaks at 177 and 212 °C [40]. In the present study, two different peaks with very low intensity were observed in the TPR profile of the Cu/TiO<sub>2</sub> catalyst at 152, and 196 °C. The broad reduction peak centered at 152 °C can be attributed to the reduction of CuO

particles being in strong interaction with the titania support. The peaks at 152 and 196 °C correspond to the reductions of Cu<sup>2+</sup> → Cu<sup>+</sup> and Cu<sup>+</sup> → Cu<sup>0</sup>, respectively. The total hydrogen volume adsorbed in Cu/TiO<sub>2</sub> is much less compared to other's and may be due to a lower amount of the Cu<sup>2+</sup> state available in the framework. This phenomenon suggests that the surface copper species exist in the metallic (Cu<sup>0</sup>) state in Cu/TiO<sub>2</sub> sample.

In the case of Fe/TiO<sub>2</sub>, the reduction proceeds in the range 220–450 °C, and the reduction transition is recorded at 333 °C;

**Table 2**  
H<sub>2</sub>Temperature programmed reduction and hydrogen consumption of transition metal modified TiO<sub>2</sub> catalyst with Ti:M' atomic ratio of 20 obtained at different temperatures.

Catalyst <sup>a</sup>	TPR reduction transitions <sup>b</sup>				H <sub>2</sub> consumption (μ mol/g of catalyst)
	Peak 1 (°C)	Peak 2 (°C)	Peak 3 (°C)	Peak4 (°C)	
FSP TiO <sub>2</sub>	511 (Ti <sup>4+</sup> to Ti <sup>3+</sup> )	–	–	–	60.2
Ce/TiO <sub>2</sub>	426 (Ti <sup>4+</sup> to Ti <sup>3+</sup> )	488.2 (Ce <sup>4+</sup> to Ce <sup>3+</sup> )	–	–	22.6
Co/TiO <sub>2</sub>	336 (Ti <sup>4+</sup> to Ti <sup>3+</sup> )	560 (Co <sup>3+</sup> to Co <sup>2+</sup> )	560 (Co <sup>3+</sup> to Co <sup>0</sup> )	–	2307.6
Cr/TiO <sub>2</sub>	228 (Ti <sup>4+</sup> to Ti <sup>3+</sup> )	265.1 (Cr <sup>6+</sup> to Cr <sup>5+</sup> )	441.3 (Cr <sup>5+</sup> to Cr <sup>3+</sup> )	538.6 (Cr <sup>3+</sup> to Cr <sup>2+/0</sup> )	1215.3
Cu/TiO <sub>2</sub>	–	151 (Cu <sup>2+</sup> to Cu <sup>+</sup> )	196.2 (Cu <sup>+</sup> to Cu <sup>0</sup> )	249.2 (Ti <sup>4+</sup> to Ti <sup>3+</sup> )	38.4
Fe/TiO <sub>2</sub>	265.1 (Ti <sup>4+</sup> to Ti <sup>3+</sup> )	333.1 (Fe <sup>3+</sup> to Fe <sup>2+</sup> )	<700 (Fe <sup>2+</sup> to Fe <sup>0</sup> )	–	205.8
Mn/TiO <sub>2</sub>	225 (Ti <sup>4+</sup> to Ti <sup>3+</sup> )	293.8 (Mn <sup>4+</sup> to Mn <sup>3+</sup> )	390 (Mn <sup>3+</sup> to Mn <sup>2.66+</sup> )	570 (Mn <sup>2.66+</sup> to Mn <sup>2+</sup> )	793.5
Mo/TiO <sub>2</sub>	262 (Ti <sup>4+</sup> to Ti <sup>3+</sup> )	331 (Mo <sup>4+</sup> to Mo <sup>3+</sup> )	–	–	1961.3
Ni/TiO <sub>2</sub>	298 (Ti <sup>4+</sup> to Ti <sup>3+</sup> )	373.7 (Ni <sup>2+</sup> to Ni <sup>0</sup> )	545.5 (Ni <sup>+</sup> to Ni <sup>0</sup> )	–	672.8
V/TiO <sub>2</sub>	343.2 (Ti <sup>4+</sup> to Ti <sup>3+</sup> )	403.8 (V <sup>5+</sup> to V <sup>4+</sup> )	–	–	38.4
Zr/TiO <sub>2</sub>	–	–	–	–	0

<sup>a</sup> Flame spray pyrolysis assisted catalysts.

<sup>b</sup> Measured from the H<sub>2</sub>-temperature programmed reduction.

this phenomenon was mainly assigned to the fraction of readily reducible ( $\text{Fe}^{3+} \rightarrow \text{Fe}^{2+}$ ) iron oxide particles. There is a peak appearing at 700 °C which could be assigned to the complete reduction of  $\text{Fe}^{2+}$  to metallic iron.

Three distinct reduction peaks are observed for the most active Mn/TiO<sub>2</sub> sample. The low temperature reduction peak at 320 °C is due to the reduction of MnO<sub>2</sub> to Mn<sub>2</sub>O<sub>3</sub>. This peak also contributes to the reduction of Ti<sup>4+</sup> to Ti<sup>3+</sup>, because at low loadings manganese enters into the titania lattice [12]. Additional peak at temperatures 515 °C are due to the reduction of Mn<sub>2</sub>O<sub>3</sub> to MnO. The TPR results revealed that the Mn/TiO<sub>2</sub> sample manganese oxide undergoes the consecutive reduction of MnO<sub>2</sub> → Mn<sub>2</sub>O<sub>3</sub> → MnO [39,40]. The TPR peak of Mo incorporated TiO<sub>2</sub> at 331 °C can be considered as the reductions of Mo<sup>6+</sup> → Mo<sup>5+</sup>.

Subsequently, the addition of NiO to the TiO<sub>2</sub> showed two distinct peaks at 373 and 547 °C. The hydrogen consumption peak at 373 °C is attributed to the transition of Ni<sup>2+</sup> → Ni<sup>+</sup> [41–43]. High temperature peak at 547 °C constitute the Ni<sup>+</sup> → Ni<sup>0</sup>. The Zr/TiO<sub>2</sub> reduction profile shows no sharp peaks. Addition of zirconia does not create any variation in the reduction pattern of TiO<sub>2</sub> catalyst. There are only marginal changes in  $T_{\max}$  positions of Zirconia species in Zr/TiO<sub>2</sub> catalyst for the studied temperature range. TPR results of these transition metal doped TiO<sub>2</sub> catalysts show that the interaction of titania with transition metal is different in each catalyst. Moreover, the reduction transition also depends on the metal dispersion, particle size, and the interaction between TiO<sub>2</sub> and the transition metal incorporated in TiO<sub>2</sub>.

### 3.5. X-ray photoelectron spectroscopy (XPS)

In order to get insight into the oxidation state of titanium and dopant-metal cations in the catalyst and to ensure the chemical compositions of the surface layer, the XPS spectra of the as-synthesized nanoparticles were recorded. For the identification of the titanium oxide phases and the relative percentages of Ti<sup>4+</sup>, Ti<sup>3+</sup> species, the overlapped Ti 2p peaks were deconvoluted into a number of peaks by searching for the optimal combination of Gaussian bands with the correlation coefficients ( $r^2$ ) above 0.99 (PeakFit, Version 4.0.6, AISN Software Inc.). The deconvoluted peaks are signed as specific Ti<sup>4+</sup>, Ti<sup>3+</sup> species in each spectrum (Figs. 6 and 7). The relative atomic percentages of Ti<sup>3+</sup>/Ti<sup>4+</sup>, Ti<sup>3+</sup>/Ti<sup>n+</sup>, and Ti/M' (M' = dopant metal) species were calculated by the area ratio of the corresponding characteristic peaks. The results are listed in Tables 3 and 4, using the XPS Peak fitting program, the XPS peak for Ti 2p of the metal-doped TiO<sub>2</sub> flame-made nanoparticles further divided into two different peaks, one centered on 458.9 ± 0.1 eV, attributed to Ti<sup>4+</sup> species, and the other centered on 458.1 ± 0.1 eV, ascribed to Ti<sup>3+</sup> species. The relative atomic percentage value of Ti<sup>3+</sup>/Ti<sup>4+</sup> characterized by XPS was significantly high for our flame-made Cr/TiO<sub>2</sub> nanoparticles (Ti<sup>3+</sup>/Ti<sup>4+</sup> = 0.89, 32.9%), whereas, other samples demonstrated poor atomic percentage value of Ti<sup>3+</sup>/Ti<sup>4+</sup> (Ti<sup>3+</sup>/Ti<sup>4+</sup> = 0.08–0.32). The existence of Ti<sup>3+</sup> species with narrow band gap is highly beneficial for the promotion of visible light-induced photocatalytic activity [44,45].

However, the peak position for Ti 2p in the Cr/TiO<sub>2</sub> sample shifts to higher binding energies than that of bare TiO<sub>2</sub> (Figs. 6 and 7). This shift suggests that a lower electron density of the TiO<sub>2</sub> surface after chromium nanoparticles interaction, this suggests a strong interaction between Cr species and flame-made TiO<sub>2</sub> nanoparticles in Cr/TiO<sub>2</sub> FSP catalyst. In the literature the Cr 2p<sub>3/2</sub>, Cr 2p<sub>1/2</sub> peaks appear at ~576.8 eV and ~586.5 eV, respectively [46–48]. As we can see from Tables 3 and 4, the position of the Cr 2p peaks shifted to lower binding energies. This occurrence indicates that the electrons migrate from the TiO<sub>2</sub> nanoparticles to chromium species, which reveals a strong interaction between Cr and TiO<sub>2</sub> nanostructure in the interface of flame-made nanoparticles. This clearly indicates

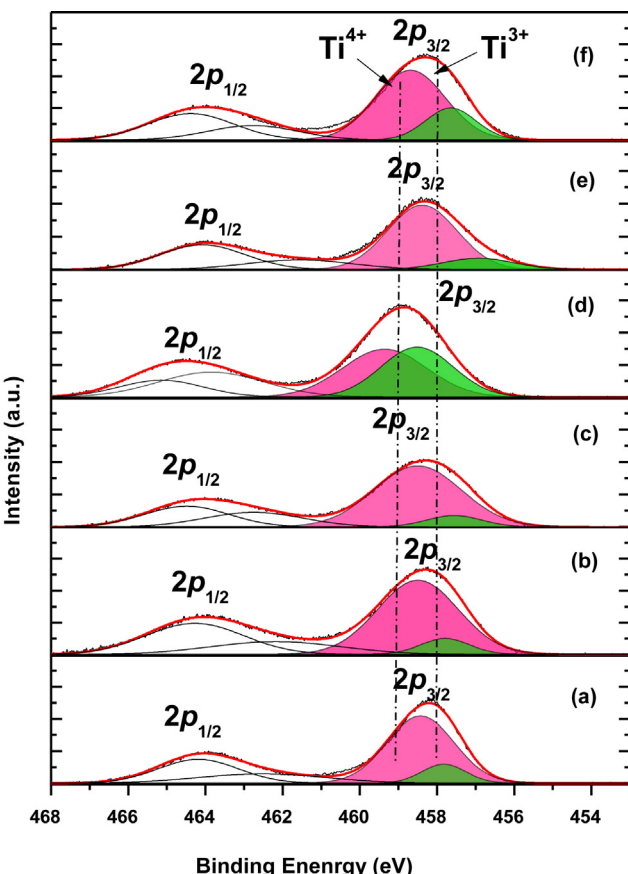


**Fig. 6.** Deconvoluted Ti 2p (XPS) spectra of (a) TiO<sub>2</sub>, (b) Ce-TiO<sub>2</sub>, (c) Co-TiO<sub>2</sub>, (d) Cr-TiO<sub>2</sub>, (e) Cu-TiO<sub>2</sub>, (f) Fe-TiO<sub>2</sub> as-prepared flame-made nanoparticles.

that the Cr/TiO<sub>2</sub> changes its structural behavior and also possible migration of oxygen atoms is taking place with respect to different structural modifications. The above analysis further verifies that which was obtained from the Ti 2p XPS spectra as shown in Figs. 6 and 7. These results are in very good agreement with our H<sub>2</sub>-TPR results where the strong interaction of Cr and TiO<sub>2</sub> established by the formation of low temperature peak (265 °C) ascribed to the Cr—O—Ti bonding.

The Cr/TiO<sub>2</sub> catalyst can absorb visible light intensely due to the surface plasmon resonance (SPR) effect [49]. Consequently, the surface electrons will be excited and electrons and holes will be separated in the Cr/TiO<sub>2</sub> system by visible light illumination, which will contribute to the significant improvement in the photoactivity in the visible light region. More significantly, the presence of Ti<sup>3+</sup> sites with narrow band gap is also a significant factor on enhancing the response of TiO<sub>2</sub> to visible region. The role of Fe<sup>3+</sup> in TiO<sub>2</sub>/Fe sample depends on the iron loading. At lower loadings, Fe<sup>3+</sup> traps photo-generated holes to form Fe<sup>4+</sup> species. These Fe<sup>4+</sup> cations react with surface OH<sup>−</sup> species to produce hydroxyl radicals resulting in the promotion of photocatalytic activity [50]. However, our Fe-TiO<sub>2</sub> catalyst (21% conversion at 100 mL min<sup>−1</sup> flow rate) demonstrated lower activity than Cr-TiO<sub>2</sub> (70.1% conversion 100 mL min<sup>−1</sup> flow rate), and better activity than other dopants. The lower conversion of Fe over Cr is due to the existence of high concentration of surface Fe<sup>3+</sup> ions, which acts as recombination site resulting in the decrease of activity [50].

Conversely, the doping of TiO<sub>2</sub> with chromium cations using flame spray pyrolysis technique leads to the production of Ti<sup>3+</sup> species. The energy level of Ti<sup>3+</sup> lies between the valence band and the conduction band of TiO<sub>2</sub>, which could effectively promote the electrons in the new valence band (VB) to be excited

**Table 3**

Binding energy, surface atomic ratio of  $\text{Ti}^{3+}/\text{Ti}^{4+}$ ,  $\text{Ti}^{3+}/\text{Ti}^{n+}$ ,  $\text{Ti}^{4+}/\text{Ti}^{n+}$ , and  $\text{Ti}/\text{M}'$  for  $\text{M}'/\text{TiO}_2$  ( $\text{M}' = \text{Ce}, \text{Co}, \text{Cu}, \text{Cr}, \text{Fe}$ , and  $\text{Ni}$ ) as-prepared catalysts determined from deconvoluted XPS spectra.

Catalyst <sup>a</sup>	Binding energy (eV)			M' <sup>b</sup>	$\text{Ti}^{3+}/\text{Ti}^{4+}$	$\text{Ti}^{3+}/\text{Ti}^{n+}$	$\text{Ti}^{4+}/\text{Ti}^{n+}$	$\text{Ti}/\text{M}'$	
	Ti 2p								
	O 1s	Ti 2p <sub>3/2</sub>	Ti 2p <sub>1/2</sub>						
TiO <sub>2</sub>	429.9	458.3	463.8	—	—	0.18	0.09	0.53	
Ce-TiO <sub>2</sub>	530.2	458.4	463.8	Ce 3d <sub>5/2</sub> 854.1	Ce 3d <sub>3/2</sub> 871.8	0.12	0.06	0.52	
Co-TiO <sub>2</sub>	530.1	458.3	463.8	Co 2p <sub>3/2</sub> 780.52	Co 2p <sub>1/2</sub> 796.32	0.11	0.07	0.58	
Cu-TiO <sub>2</sub>	530.0	458.3	463.7	Cu 2p <sub>3/2</sub> 934.1	Cu 2p <sub>1/2</sub> 941.8	0.18	0.09	0.53	
Cr-TiO <sub>2</sub>	530.5	458.7	464.3	Cr 2p <sub>3/2</sub> 576.5	Cr 2p <sub>1/2</sub> 586.2	0.89	0.30	4.56	
Fe-TiO <sub>2</sub>	530.1	458.3	463.9	Fe 2p <sub>3/2</sub> 711.8	Fe 2p <sub>1/2</sub> 723.6	0.32	0.15	0.49	
Ni-TiO <sub>2</sub>	530.3	458.4	463.8	Ni 2p <sub>3/2</sub> 855.8	Ni 2p <sub>1/2</sub> 869.7	0.16	0.09	0.57	

<sup>a</sup> Flame spray pyrolysis assisted catalysts.

<sup>b</sup> Binding energy of various dopant metals (M') from the XPS studies.

<sup>c</sup> Relative amounts are according to the metal atomic percentages from the XPS analysis.

to the conduction band of  $\text{TiO}_2$  [51]. Therefore, the existence of  $\text{Ti}^{3+}$  species on the surface that makes  $\text{TiO}_2$  excited under visible illumination. The chromium nanoparticles could serve as trapping centers for electrons photo-induced in the conduction band of  $\text{TiO}_2$ , meanwhile leaving the holes in the valence band of  $\text{TiO}_2$ . These results imply that the migration of charges is prompted on the interface of metal-doped  $\text{TiO}_2$  flame-made nanoparticles and the recombination of photo-induced  $e^-/h^+$  pairs is suppressed by the well-known Schottky barrier effect, which will contribute to the enhancement of photocatalytic activity. Napoli et al. [52] also observed a reversible electron transfer between the dopant metal and  $\text{Ti}^{3+}$  centers forming the diamagnetic bulk species. The authors [52] also claimed that the formation of diamagnetic bulk species is

more favorable with an increase in  $\text{Ti}^{3+}$  and that is the key for the improvement in the visible light photocatalytic activity.

### 3.6. Photocatalytic performance of $M/\text{TiO}_2$ catalysts in visible region

In the present work, we operated the reactor in plug flow condition where the reactant species are making single pass through the reactor. Here, the independent variable is the molar flow rate and is varied by holding the inlet concentration ( $C_{AO}$ ) constant and varying the volumetric flow rate. The dependent variable is the fractional conversion. Assuming that the photocatalytic oxidation of acetonitrile follows a power law model, the reactor design equation is (Eq. (3)),

$$\frac{W}{F_{AO}} = \int_{f_{AO}}^{f_A} \frac{df_A}{-r_A} \quad (3)$$

where  $-r_A$  is the rate of disappearance of acetonitrile,  $W$  is the mass of the catalyst,  $F_{AO}$  is the molar flow rate of acetonitrile entering the reactor and  $f_{AO}$  and  $f_A$  are the fractional conversions of  $A$ . Where,  $f_{AO} = 0$  and  $f_A = 1 - (C_A/C_{AO})$ ,  $C_{AO}$  and  $C_A$  inlet and out concentrations of the reactant. By taking first order photodegradation reaction and integrating the above equation we get (Eq. (4)).

$$\ln(1 - f_A) = -K_A C_{AO} \frac{W}{F_{AO}} \quad (4)$$

By plotting the graph of  $\ln(1 - f_A)$  vs  $W/F_{AO}$  we have got the rate constant  $K_A$  ( $\text{m}^3 \text{g}^{-1} \text{s}^{-1}$ ). On the basis of the surface characterization results described above, it is now instructive to compare the photocatalytic activities of all as-prepared metal-doped  $\text{TiO}_2$  materials. Fig. 7 shows the conversion of acetonitrile with respective increasing flow rate values for photo degradation over transition metal incorporated  $\text{TiO}_2$  under visible light. We have noticed the photo degradation of P25 under visible light. This could be attributed to the excitation of rutile (absorption threshold 414 nm). It is worth understanding that despite inactivation of anatase (absorption threshold 388 nm) under visible light, it does not rule out the possibility of photo generated charge transfer between the two crystallite phases, hence allowing for photocatalytic reaction to take place on anatase surface [53].

We can observe that the Cr-incorporated catalyst is much more active than the other transition metal incorporated catalysts. The catalyst showed no deactivation as usually photooxidized acetonitrile, because the amount of active oxygen species for oxidation was kept constant during photooxidation. The visible light provided enough energy for the electrons to leap from the valence band to the conduction band and  $\text{Cr}^{6+}$  acts as an intermediate level for electron excitation under visible light. It is based on the sensitization of titania with a tetrahedrally coordinated transition metal oxide, which

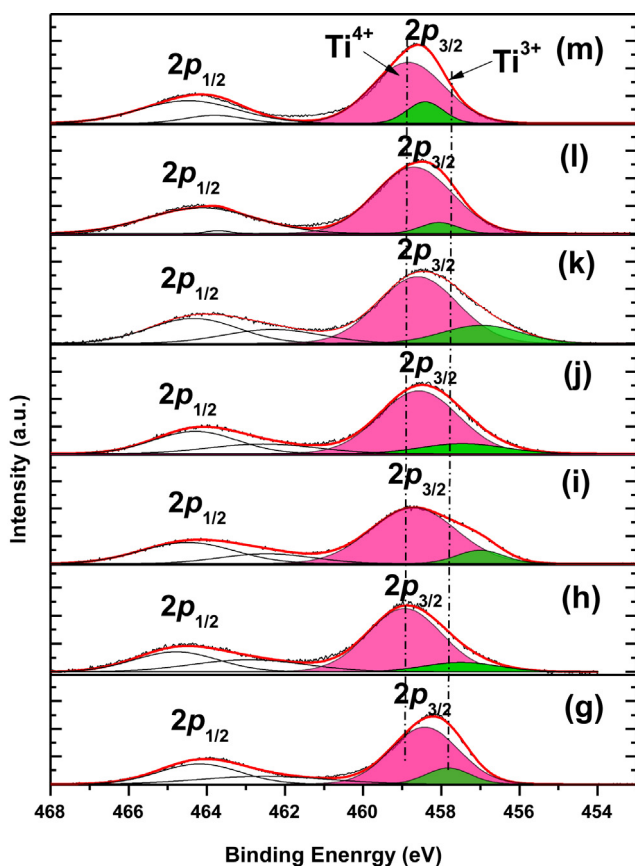


**Fig. 7.** Deconvoluted Ti 2p (XPS) spectra of (g)  $\text{TiO}_2$  (h)  $\text{Mn}-\text{TiO}_2$ , (i)  $\text{Mo}-\text{TiO}_2$ , (j)  $\text{Ni}-\text{TiO}_2$ , (k)  $\text{V}-\text{TiO}_2$ , (l)  $\text{Y}-\text{TiO}_2$ , and (m)  $\text{Zr}-\text{TiO}_2$  as-prepared flame-made nanoparticles.

**Table 4**

Binding energy, surface atomic ratio of  $\text{Ti}^{3+}/\text{Ti}^{4+}$ ,  $\text{Ti}^{3+}/\text{Ti}^{n+}$ ,  $\text{Ti}^{4+}/\text{Ti}^{n+}$ , and  $\text{Ti}/\text{M}'$  for  $\text{M}'/\text{TiO}_2$  ( $\text{M}' = \text{V}, \text{Mn}, \text{Mo}, \text{Y}, \text{and Zr}$ ) as-prepared catalysts determined from deconvoluted XPS spectra.

Catalyst <sup>a</sup>	Binding energy (eV)			$\text{M}'^{\text{b}}$	$\text{Ti}^{3+}/\text{Ti}^{4+}$	$\text{Ti}^{3+}/\text{Ti}^{n+}$	$\text{Ti}^{4+}/\text{Ti}^{n+}$	$\text{Ti}/\text{M}'^{\text{c}}$	
	Ti 2p								
	O 1s	Ti 2p <sub>3/2</sub>	Ti 2p <sub>1/2</sub>						
$\text{TiO}_2$	429.9	458.3	463.8	—	—	0.18	0.09	0.53	
V-TiO <sub>2</sub>	530.0	458.3	463.7	$\text{V } 2p_{3/2} 516.9$	$\text{V } 2p_{1/2} 520.1$	0.26	0.13	0.51	
Mn-TiO <sub>2</sub>	530.1	458.8	464.2	$\text{Mn } 2p_{3/2} 642.6$	$\text{Mn } 2p_{1/2} 653.5$	0.14	0.08	0.56	
Mo-TiO <sub>2</sub>	530.1	458.5	464.0	$\text{Mo } 3d_{5/2} 233.2$	$\text{Mo } 3d_{3/2} 236.5$	0.12	0.07	0.57	
Y-TiO <sub>2</sub>	530.2	458.6	464.1	$\text{Y } 3d_{5/2} 157.6$	$\text{Y } 3d_{3/2} 159.5$	0.08	0.05	0.61	
Zr-TiO <sub>2</sub>	530.1	458.7	464.2	$\text{Zr } 3d_{5/2} 181.8$	$\text{Zr } 3d_{3/2} 184.1$	0.17	0.09	0.56	
								20.4	

<sup>a</sup> Flame spray pyrolysis assisted catalysts.

<sup>b</sup> Binding energy of various dopant metals ( $\text{M}'$ ) from the XPS studies.

<sup>c</sup> Relative amounts are according to the metal atomic percentages from the XPS analysis.

can scavenge electrons from the valence band and release electrons to the conduction band upon the excitation by visible light, thus bringing about charge separation. The charges can then react with the adsorbed oxygen and surface hydroxyl groups, producing reactive oxygen species. Although Fe, Mn, V, Co and Ni incorporated materials absorb visible light (Fig. 4), their photocatalytic activity is very low under visible light (Fig. 8). The lower activity of these catalysts when compared with Cr/TiO<sub>2</sub> can be explained by their inability to act as energy level for electrons created in TiO<sub>2</sub> to leap. Mn<sup>3+</sup> is combined effectively with TiO<sub>2</sub> because its surface metal dispersion was kept high after TiO<sub>2</sub> loading. Mn<sup>3+</sup> incorporated catalyst was inactive because of the small energy driving force for electrons to detrap from Mn<sup>2+</sup>. As mentioned above, the interaction of titania loaded and transition metal ions in our samples creates a plurality of surface defects, which increases the probability of recombination of the light induced charges. Therefore, the activity of  $\text{M}'\text{-TiO}_2$  ( $\text{M}' = \text{Mn}, \text{Co}, \text{Cu}, \text{Ni}, \text{and Mo}$ ) is low. Photocatalytic degradation of the acetonitrile in the present work had followed a pseudo first order kinetics. The rate constants of the various metal-doped TiO<sub>2</sub> calculated by using Eq. (3) are given in Table 3. As we can observe from the table, among all the  $\text{M}'/\text{TiO}_2$ , Cr modified TiO<sub>2</sub> demonstrated a superior photocatalytic activity and the rate constant is about many folds higher than the rest of the metal doped catalysts. Along with Cr, Fe and V doped TiO<sub>2</sub> also showed a significant photocatalytic activity in visible light.

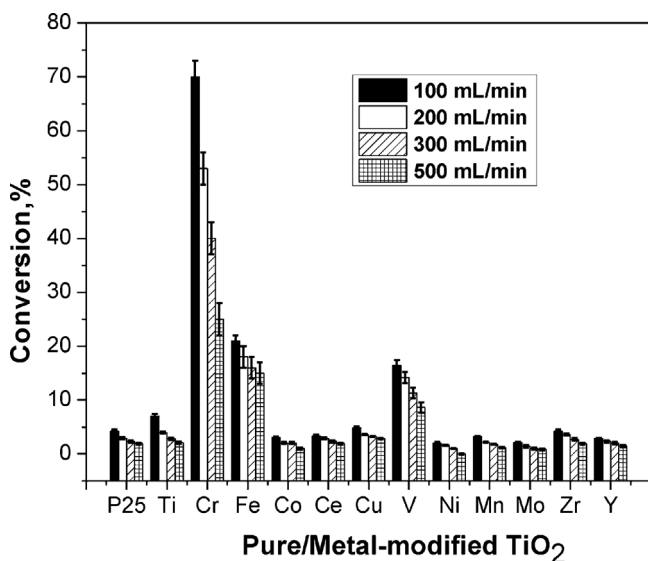


**Fig. 8.** Photocatalytic conversion of  $\text{M}'/\text{TiO}_2$  with the steady 500 ppm concentration of acetonitrile with 50 mg of catalyst loading on to the reactor.

**Table 5**  
Photocatalytic activity of the catalyst used in the present study.

Catalyst	Absorption region	Band gap (eV)	$K_A (\text{m}^3 \text{g}^{-1} \text{s}^{-1})$
P25	UV	3.11	0.051
FSP TiO <sub>2</sub>	UV	3.08	0.098
Ce/TiO <sub>2</sub>	UV	3.13	0.014
Co/TiO <sub>2</sub>	Visible	2.54	0.021
Cr/TiO <sub>2</sub>	Visible	2.82	0.616
Cu/TiO <sub>2</sub>	Visible	2.86	0.010
Fe/TiO <sub>2</sub>	Visible	2.69	0.152
Mn/TiO <sub>2</sub>	Visible	2.86	0.006
Mo/TiO <sub>2</sub>	UV	3.19	0.004
Ni/TiO <sub>2</sub>	Visible	2.37	0.019
V/TiO <sub>2</sub>	Visible	2.63	0.165
Y/TiO <sub>2</sub>	UV	3.20	0.004
Zr/TiO <sub>2</sub>	UV	3.21	0.008

Taking FSP titania as the base in Fig. 9 we can observe that the metals which have promoting effect on the photocatalytic degradation of acetonitrile in visible region are Cr, Fe and V. The incorporation of the other transition metals (Mn, Mo, Ce, Co, Cu, Ni, Y and Zr) has inhibition effect on the photocatalytic activity of the catalyst in visible region (Table 5). Even though some of these metals have shown visible light absorption they fail to have catalytic activity this may be caused by the metals covering the surface of the titania particles. The photocatalytic activity of the catalyst was observed in the following order  $\text{Cr/TiO}_2 \gg \text{Fe/TiO}_2 > \text{V/TiO}_2$ ,

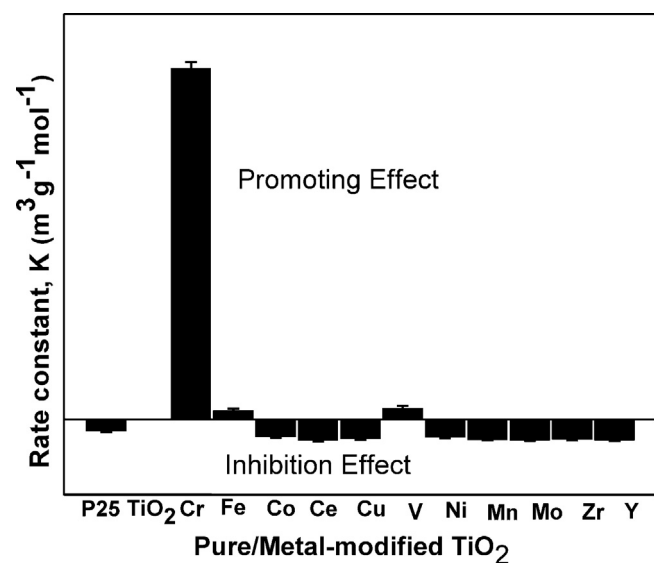


**Fig. 9.** The promoter and inhibition effect of the pure/metal modified  $\text{TiO}_2$ .

other metals has shown very negligible photocatalytic activity in gas phase visible light degradation of acetonitrile.

#### 4. Conclusions

A number of transition metal ( $M' = V, Cr, Fe, Co, Mn, Mo, Ni, Cu, Y, Ce$ , and  $Zr$ ) incorporated  $TiO_2$  ( $Ti/M' = 20$  atomic ratio) materials were synthesized by flame aerosol pyrolysis method. The characterization results showed enhancement of the absorption in visible light by some composite materials (Cr, Fe, V, Cu, Mn, Co, and Ni). The photocatalytic activity of the materials in visible light for the degradation of gas phase acetonitrile was also tested. Only Cr doped  $TiO_2$  exhibited considerable activity in visible light. Other materials did not show significant activity in visible light. The strong interaction (formation of (Cr—O—Ti) bonds) is the main reason that Cr/ $TiO_2$  is an active photocatalyst in visible light. The enhancement of photocatalytic activities of the Cr-doped  $TiO_2$  flame-made nanoparticles is mainly attributed to the interaction between Ti and Cr species. In particular, the surface plasmas on resonances of Cr nanoparticles excited by visible light as well as the presence of dominant  $Ti^{3+}$  in Cr/ $TiO_2$  also contribute to their higher photocatalytic properties. The photocatalytic activity of the catalyst was observed in the following order Cr/ $TiO_2$  > Fe/ $TiO_2$  > V/ $TiO_2$ , other metals has shown very negligible photocatalytic activity in gas phase visible light degradation of acetonitrile.

#### Acknowledgement

The authors wish to acknowledge EPA/Pegasus contract (contract number EP-C-11-006) for financial support of this work through the scholarship to Siva Nagi Reddy Inturi.

#### References

- [1] A. Fujishima, K. Honda, *Nature* 238 (1972) 37–38.
- [2] J. Peral, X. Domenech, D.F. Ollis, *Journal of Chemical Technology and Biotechnology* 70 (1978) 117.
- [3] D.F. Ollis, *ACS Symposium Series* 518, American Chemical Society, Washington, DC, 1993.
- [4] M.R. Hoffmann, S.T. Martin, W.Y. Choi, D.W. Bahnemann, *Chemical Reviews* 95 (1995) 69–96.
- [5] R.W. Matthews, *Water Research* 24 (1990) 653.
- [6] M.A. Fox, M.T. Dulay, *Chemical Reviews* 93 (1993) 341–357.
- [7] M. Anpo, M. Takeuchi, *Journal of Catalysis* 216 (2003) 505–516.
- [8] R. Asahi, T. Morikawa, T. Ohwaki, K. Aoki, Y. Taga, *Science* 293 (2001) 269–271.
- [9] Y.M. Xu, C.H. Langford, *Journal of Physical Chemistry* 99 (1995) 11501–11507.
- [10] J.C. Yu, G.S. Li, X.C. Wang, X.L. Hu, C.W. Leung, Z.D. Zhang, *Chemical Communications* (2006) 2717.
- [11] L. Davydov, E.P. Reddy, P. France, P.G. Smirniotis, *Journal of Catalysis* 203 (2001) 157–167.
- [12] E.P. Reddy, B. Sun, P.G. Smirniotis, *Journal of Physical Chemistry B* 108 (2004) 17198–17205.
- [13] S.V. Awate, N.E. Jacob, S.S. Deshpande, T.R. Gaydhankar, A.A. Belhekar, *Journal of Molecular Catalysis A* 226 (2005) 149–154.
- [14] V.R. Elias, E.G. Vaschetto, K. Sapag, M.E. Crivello, S.G. Casuscelli, G.A. Eimer, *Topics in Catalysis* 54 (2011) 277–286.
- [15] F.C. Marques, M.C. Canela, A.M. Stumbo, *Catalysis Today* 133 (2008) 594–599.
- [16] B. Sun, E.P. Reddy, P.G. Smirniotis, *Applied Catalysis B: Environmental* 57 (2005) 139–149.
- [17] L. Madler, *KONA* 22 (2004) 107–120.
- [18] R. Strobel, A. Baiker, S.E. Pratsinis, *Advanced Powder Technology* 17 (2006) 457.
- [19] J. Sanjeev, D.J. Skamser, T.T. Kodas, *Aerosol Science and Technology* 27 (1997) 575.
- [20] D. Vollath, V.D. Szabo, J. Hausselt, *Journal of the European Ceramic Society* 17 (1997) 1317.
- [21] T. Sasaki, Y. Shimizu, N. Koshizaki, *Journal of Photochemistry and Photobiology A: Chemistry* 182 (2006) 335.
- [22] K.L. Choy, *Progress in Materials Science* 48 (2003) 57.
- [23] S.E. Pratsinis, *Progress in Energy and Combustion* 24 (1998) 197–219.
- [24] G. Byrd, K. Fowler, R. Hicks, M. Lovette, M. Borgerding, *Journal of Chromatography A* 503 (1990) 359–436.
- [25] L. Madler, H.K. Kammer, R. Mueller, S.E. Pratsinis, *Aerosol Science* 33 (2002) 369–389.
- [26] W.Y. Teoh, L. Madler, D. Beydoun, S.E. Pratsinis, R. Amal, *Chemical Engineering Science* 60 (2005) 5852–5861.
- [27] W.J. Stark, L. Madler, M. Maciejewski, S.E. Pratsinis, A. Baiker, *Chemical Communications* (2003) 588–589.
- [28] W.J. Stark, S.E. Pratsinis, US Patent, US2006229197, 2006.
- [29] W.J. Stark, L. Madler, S.E. Pratsinis, US Patent, US20030602305, 2003.
- [30] R. Jenkins, R.L. Snyder, *Introduction to X-ray Powder Diffractometry*, Wiley & Sons, Inc., New York, 1996.
- [31] Z.D. Zhu, Z.X. Chang, L.J. Kevan, *Journal of Physical Chemistry B* 103 (1999) 2680–2689.
- [32] W.J. Stark, K. Wegner, S.E. Pratsinis, A. Baiker, *Journal of Catalysis* 197 (2001) 182.
- [33] S. Nahar, K. Hasegawa, S. Kagaya, *Chemosphere* 65 (2006) 1976.
- [34] J.F. Zhu, F. Chen, J.L. Zhang, H.J. Chen, M. Anpo, *Journal of Photochemistry and Photobiology A: Chemistry* 180 (2006) 196.
- [35] S. Klosek, D. Raftery, *Journal of Physical Chemistry B* 105 (2001) 2815.
- [36] Z. Zhu, M. Hartman, E. Maes, R.S. Czernuszewicz, L. Kevan, *Journal of Physical Chemistry B* 104 (2000) 4690.
- [37] H.C. Yao, Y.F. Yu Yao, *Journal of Catalysis* 86 (1984) 254–264.
- [38] B. Jongsomjit, C. Sakkamnuson, J.G. Goodwin Jr., P. Praserthdam, *Catalysis Letters* 94 (2004) 209–215.
- [39] A. Rahman, M. Ahmed, in: M. Absi-Halabi, J. Besbara, H. Qabazard, A. Stanislau (Eds.), *Catalysts in Petroleum Refining and Petrochemical Industries*, Elsevier, Amsterdam, 1995, pp. 419–426.
- [40] F. Bocuzzi, A. Chiorino, G. Martra, M. Gargano, N. Ravasio, B. Carrozzin, *Journal of Catalysis* 165 (1997) 129–139.
- [41] B. Thirupathi, P.G. Smirniotis, *Journal of Catalysis* 288 (2012) 74–83.
- [42] H.W. Chen, Y. Ku, Y.L. Kuo, *Chemical Engineering and Technology* 30 (2007) 1242–1247.
- [43] B. Thirupathi, P.G. Smirniotis, *Catalysis Letters* 141 (2011) 1399–1404.
- [44] P.M. Sreekanth, P.G. Smirniotis, *Catalysis Letters* 122 (2008) 37–42.
- [45] C. Su, L. Liu, M. Zhang, Y. Zhang, C. Shao, *CrystEngComm* 14 (2012) 3989–3999.
- [46] B. Wang, J. Iqbal, X. Shan, G. Huang, H. Fu, R. Yu, D. Yu, *Materials Chemistry and Physics* 113 (2009) 103–106.
- [47] A.B. Gaspar, C.A.C. Perez, L.C. Dieguez, *Applied Surface Science* 252 (2005) 939–949.
- [48] Y. Liu, J. Yang, Q. Guan, L. Yang, H. Liu, Y. Zhang, Y. Wang, D. Wang, J. Lang, Y. Yang, L. Fei, M. Wei, *Applied Surface Science* 256 (2010) 3559–3562.
- [49] H.H. Chien, H.C. Wu, *Micro & Nano Letters* 10 (2012) 1033–1037.
- [50] J. Zhang, T. Tong, B. Tian, F. Chen, D. He, *Journal of Hazardous Materials* 155 (2008) 572–579.
- [51] J.X. Li, J.H. Xu, W.L. Dai, *Journal of Physical Chemistry C* 113 (2009) 8343–8349.
- [52] F. Napoli, M. Chiesa, S. Livraghi, E. Giannello, S. Agnoli, G. Granozzi, G. Pacchioni, C.D. Valentini, *Chemical Physics Letters* 477 (2009) 135–138.
- [53] D.C. Hurum, G.A. Alexander, K.A. Gray, *Journal of Physical Chemistry B* 107 (2003) 4545–4549.